

Frustration of square cupola in $\text{Sr}(\text{TiO})\text{Cu}_4(\text{PO}_4)_4$

S. S. Islam,¹ K. M. Ranjith,² M. Baenitz,² Y. Skourski,³ A. A. Tsirlin,^{4,*} and R. Nath^{1,†}

¹*School of Physics, Indian Institute of Science Education and Research Thiruvananthapuram-695016, India*

²*Max Planck Institut für Chemische Physik fester Stoffe,
Nothnitzer Strasse 40, 01187 Dresden, Germany*

³*Dresden High Magnetic Field Laboratory, Helmholtz-Zentrum Dresden-Rossendorf, 01314 Dresden, Germany*

⁴*Experimental Physics VI, Center for Electronic Correlations and Magnetism,
University of Augsburg, 86135 Augsburg, Germany*

(Dated: May 22, 2018)

The structural and magnetic properties of the square-cupola antiferromagnet $\text{Sr}(\text{TiO})\text{Cu}_4(\text{PO}_4)_4$ are investigated via x-ray diffraction, magnetization, heat capacity, and ^{31}P nuclear magnetic resonance experiments on polycrystalline samples, as well as density-functional band-structure calculations. The temperature-dependent unit cell volume could be described well using the Debye approximation with the Debye temperature of $\theta_D \simeq 550$ K. Magnetic response reveals a pronounced two-dimensionality with a magnetic long-range-order below $T_N \simeq 6.2$ K. High-field magnetization exhibits a kink at $1/3$ of the saturation magnetization. Asymmetric ^{31}P NMR spectra clearly suggest strong in-plane anisotropy in the magnetic susceptibility, as anticipated from the crystal structure. From the ^{31}P NMR shift vs bulk susceptibility plot, the isotropic and axial parts of the hyperfine coupling between ^{31}P nuclei and the Cu^{2+} spins are calculated to be $A_{\text{hf}}^{\text{iso}} \simeq 6539$ and $A_{\text{hf}}^{\text{ax}} \simeq 952$ Oe/ μ_B , respectively. The low-temperature and low-field ^{31}P NMR spectra indicate a commensurate antiferromagnetic ordering. Frustrated nature of the compound is inferred from the temperature-dependent ^{31}P NMR spin-lattice relaxation rate and confirmed by our microscopic analysis that reveals strong frustration of the square cupola by next-nearest-neighbor exchange couplings.

PACS numbers: 75.50.Ee, 75.40.Cx, 75.10.Jm, 75.30.Et

I. INTRODUCTION

Recently, two new chiral compounds $A(\text{TiO})\text{Cu}_4(\text{PO}_4)_4$ ($A = \text{Ba}$ and Sr) (abbreviated as BTCPO and STCPO, respectively) were synthesized [1]. Both the compounds crystallize in the tetragonal space group $P4_212$ with the lattice parameters [$a = 9.6028(5)$ Å and $b = 7.1209(5)$ Å] and [$a = 9.5182(5)$ Å and $b = 7.0087(5)$ Å], respectively. BTCPO and STCPO feature a quasi-two-dimensional (2D) structure, which is formed by the upward and downward Cu_4O_{12} cluster-assembly units with alternating orientations in the ab -plane, as depicted in Fig. 1(a). Each Cu_4O_{12} unit consists of four corner-sharing CuO_4 square plaquettes forming a non-coplanar structure called (irregular) *square – cupola*. Two types of the square-cupola units (upward and downward) are present in the structure [see Fig. 1(b)]. Each upward Cu_4O_{12} square cupola is connected to the nearest downward square cupola unit and with the nearest upward TiO_5 square pyramid [located on top (or bottom) of each upward (or downward) Cu_4O_{12} square-cupola unit] by the PO_4 tetrahedra.

A detailed magnetoelectric study has been reported for BTCPO via magnetization, heat capacity, dielectric, neutron scattering experiments, and subsequent model

calculations [2–5]. A huge anomaly in the temperature-dependent dielectric constant was observed at the Néel temperature $T_N \simeq 9.5$ K in the magnetic field applied along the [100] and $[1\bar{1}0]$ directions. It has been proposed that the asymmetric square-cupola units in the crystal structure can sustain magnetoelectric-active multipole moments associated with an antiferro magnetic quadrupole order. Later, a combined experimental [high-field magnetization measurement] and theoretical [cluster mean-field approximation] study [3] interpreted the magnetoelectric phase diagram and analyzed microscopically how the asymmetric square-cupola units trigger the magnetoelectric response through anisotropic exchange interactions. The critical role of the in-plane component of the Dzyaloshinsky-Moriya (DM) interaction, induced by the non-coplanar structure of the square cupola was established. The non-collinear magnetic structure of BTCPO has been determined using neutron diffraction and, eventually, spherical neutron polarimetry [5].

Interestingly, the degree of chirality can be tuned in the $A(\text{BO})\text{Cu}_4(\text{PO}_4)_4$ ($B = \text{Ti}$ and V) series of compounds by changing both the A and B cations. For example, the structural chirality is more pronounced in STCPO compared BTCPO [1]. We therefore investigated and report below the magnetic behavior of STCPO, as revealed by different experimental techniques and *ab initio* calculations.

* altsirlin@gmail.com

† rnath@iisertvm.ac.in

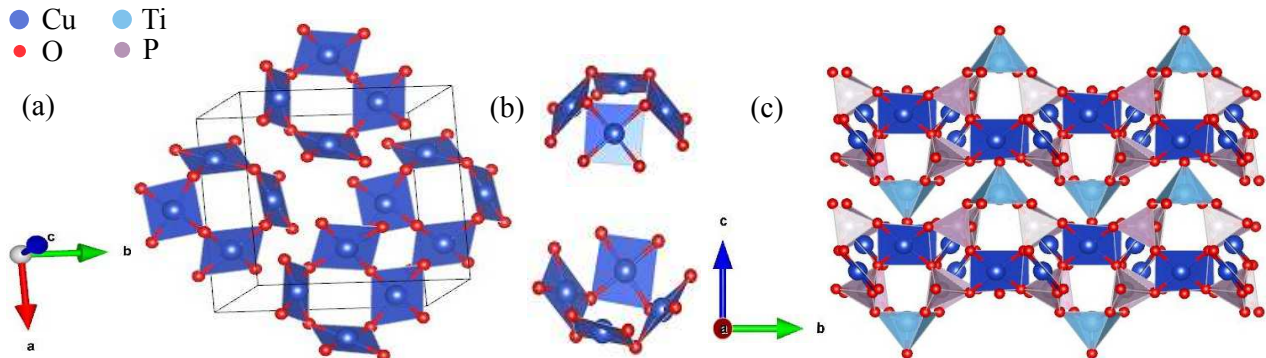


FIG. 1. (a) Crystal structure of Sr(TiO)Cu₄(PO₄)₄ viewed along with the three principal axes in the left. The Cu and O ions are shown by the blue and red spheres, respectively. The CuO₄ planes (plaquettes) within the up/down square cupola are shown in blue. The black outline represents the unit cell. (b) The upward and downward Cu₄O₁₂ square cupola are shown. (c) Crystal structure of Sr(TiO)Cu₄(PO₄)₄ along the *a*-axis. The Ti and P atoms are shown by cyan and grey spheres, respectively.

II. METHODS

Polycrystalline sample of STCPO was synthesized by the conventional solid-state reaction technique. The synthesis involves two steps. In the first step, the initial reactants SrCO₃ (Aldrich, 99.995%), CuO (Aldrich, 99.999%), TiO₂ (Aldrich, 99.9%), and (NH₄)H₂PO₄ (Aldrich, 99%) were taken in stoichiometric ratios, ground thoroughly, and pressed into pellets. The pellets were kept in a quartz crucible and fired at 300 °C for 12 hours in air to remove NH₃ and CO₂ from the sample. In the second step, the sample was re-ground, pelletized, and annealed at 950 °C for 24 hours in air in a platinum crucible. Phase purity of the sample was confirmed by powder x-ray diffraction (XRD) measurements using the diffractometer from PANalytical (CuK_α radiation, λ_{avg} ≈ 1.5418 Å). The temperature-dependent powder XRD experiments were carried out over a broad temperature range (15 K ≤ *T* ≤ 650 K) using the Oxford Phenix (for low temperatures) and Anton-Paar HTK 1200N (for high temperatures) attachments.

Magnetization (*M*) measurements were performed using the vibrating sample magnetometer (VSM) attachment to the Physical Property Measurement System (PPMS, Quantum Design). Heat capacity (*C_p*) was measured using the heat capacity option in the PPMS, adopting the relaxation technique. High-field magnetization measurement up to 60 T was performed at the Dresden High Magnetic Field Laboratory using pulsed fields. Details of the measurement procedure are described in Ref. [6].

The NMR measurements were carried out using pulsed NMR techniques on ³¹P (nuclear spin *I* = 1/2 and gyromagnetic ratio γ_N/2π = 17.237 MHz/T) nuclei. We have carried out the measurements at two different radio frequencies of 70.41 MHz and 25 MHz, which correspond to the applied fields of about 4.085 T and 1.45 T, respectively. The spectra were obtained by sweeping the field at a fixed frequency. The NMR shift *K*(*T*) =

(*H*_{ref} − *H*(*T*))/*H*(*T*) was determined by measuring the resonance field of the sample [*H*(*T*)] with respect to the nonmagnetic reference H₃PO₄ (resonance field *H*_{ref}). The ³¹P spin-lattice relaxation rate 1/*T*₁ was measured by the conventional inversion recovery method.

Exchange couplings *J*_{*ij*} of the spin Hamiltonian

$$H = \sum_{\langle ij \rangle} J_{ij} \mathbf{S}_i \mathbf{S}_j, \quad (1)$$

where the summation is over all pairs *ij*, were obtained from density-functional (DFT) band-structure calculations performed in the full-potential local-orbital FPLO code [7] using Perdew-Burke-Ernzerhof flavor of the exchange-correlation potential [8]. First Brillouin zone was sampled by a *k*-mesh with up to 216 points in the symmetry-irreducible part. Exchange couplings were extracted using two complementary approaches. On one hand, the uncorrelated band structure was parametrized by a tight-binding model, and exchange couplings were estimated via the hopping parameters. On the other hand, total energies from DFT+*U* calculations were used in a mapping procedure [9]. In DFT+*U*, electronic correlations in the Cu 3*d* shell are accounted for on the mean-field level using the on-site Coulomb repulsion *U*_{*d*} = 9.5 eV and Hund's coupling *J*_{*d*} = 1 eV [10–12].

For simulating magnetic susceptibility and magnetization, finite lattices with up to 4 square cupolas and periodic boundary conditions were used. The simulations were performed using the `fulldiag` routine of the ALPS package [13].

III. RESULTS AND DISCUSSION

A. Crystal structure

In order to check the phase purity and to detect structural transitions, if any, powder XRD was measured at different temperatures. Le-Bail fits of the XRD patterns

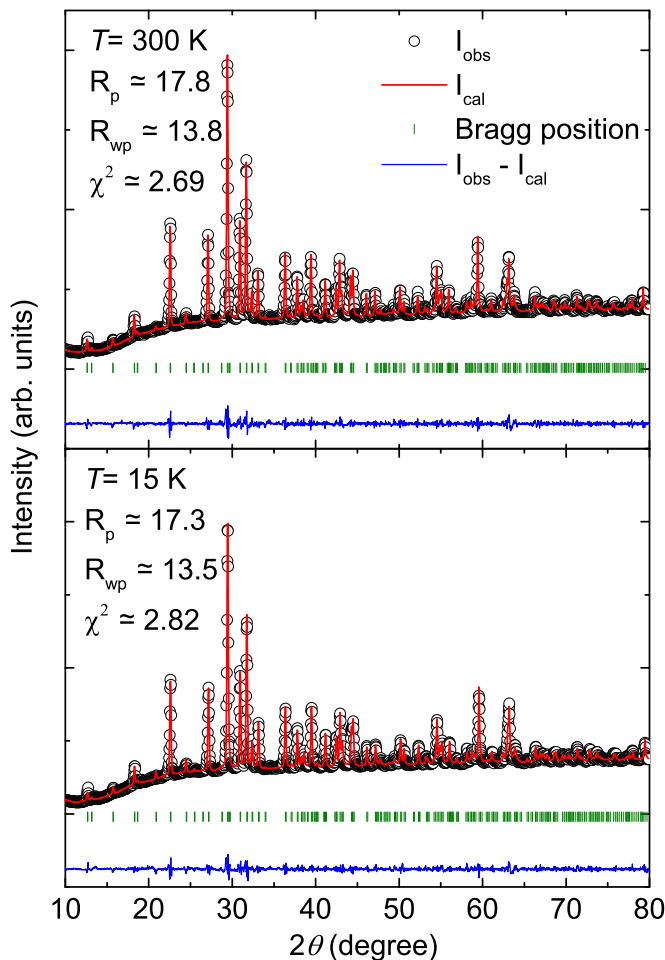


FIG. 2. X-ray diffraction data collected at $T = 300$ K and 15 K. The solid lines denote the Le-Bail fit of the data. The Bragg peak positions are indicated by green vertical bars, the bottom blue line indicates the difference between the experimental and calculated intensities.

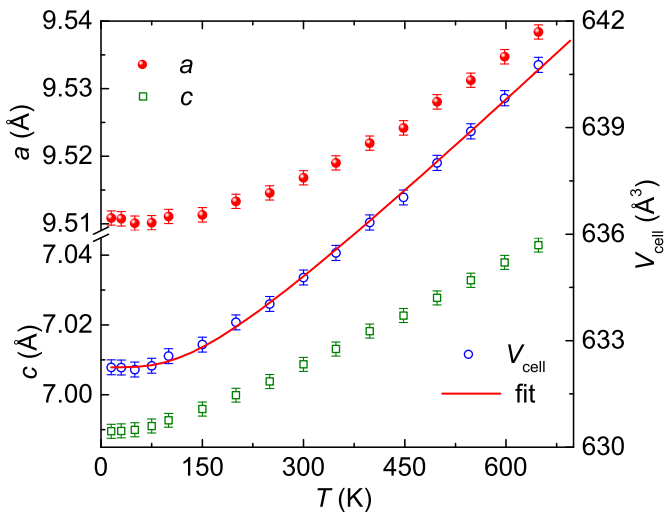


FIG. 3. Variation of lattice constants (a and c) and unit cell volume (V_{cell}) with temperature. The solid line represents the fit of $V_{\text{cell}}(T)$ by Eq. (2).

were carried out using the FullProf package.[14] The initial structural parameters for this purpose were taken from Ref. [1]. Figure 2 shows the powder XRD patterns at 300 K and 15 K along with the fits. The absence of unindexed peaks confirms phase purity of our sample. The obtained lattice constants and volume of the unit cell (V_{cell}) at room temperature are $a = 9.5168(1)$ Å, $c = 7.0087(1)$ Å, and $V_{\text{cell}} \simeq 634.78(2)$ Å³, which are consistent with the previous report [1]. Figure 3 displays the temperature variation of lattice constants and unit cell volume. No structural transition was observed down to 15 K. The lattice constants and V_{cell} were found to decrease systematically upon cooling. The temperature variation of V_{cell} was fitted by the equation [15]

$$V(T) = \gamma U(T)/K_0 + V_0, \quad (2)$$

where V_0 is the cell volume at $T = 0$ K, K_0 is the bulk modulus, and γ is the Grüneisen parameter. $U(T)$ is the internal energy which can be expressed in terms of the Debye approximation as

$$U(T) = 9p k_B T \left(\frac{T}{\theta_D} \right)^3 \int_0^{\theta_D/T} \frac{x^3}{e^x - 1} dx. \quad (3)$$

Here, p is the number of atoms in the unit cell, and k_B is the Boltzmann constant. Using this approximation (see Fig. 3), the Debye temperature (θ_D) and other parameters were estimated to be $\theta_D \simeq 550$ K, $\gamma/K_0 \simeq 2.68 \times 10^{-5}$ Pa⁻¹, and $V_0 \simeq 632.2$ Å³.

B. Magnetization

The static magnetic susceptibility $\chi(T)$ ($\equiv M/H$) of the polycrystalline STCPO sample measured as a function of temperature at different applied fields $H = 0.5$ T and 3 T is shown in the upper panel of Fig. 4. At high temperatures, $\chi(T)$ increases with decreasing temperature in a Curie-Weiss manner and passes through a broad maximum around $T_{\chi}^{\text{max}} \simeq 10$ K. This broad maximum is indicative of a short-range order, anticipated for low-dimensional antiferromagnetic (AFM) spin systems. The temperature corresponding to the broad maximum is a measure of the dominant AFM exchange coupling. Below T_{χ}^{max} , $\chi(T)$ exhibits a small kink at $T_N \simeq 6.2$ K, a possible indication of magnetic long-range ordering (LRO). In order to see this feature, we plotted temperature derivative of χ in the inset of Fig. 4. It shows a clear anomaly at $T_N \simeq 6.2$ K. At very low temperatures, $\chi(T)$ shows an upturn, which is suppressed with the applied magnetic field. This upturn could be due to a small amount of extrinsic paramagnetic impurities and/or defects present in the sample.

For a quantitative analysis, the high-temperature $\chi(T)$ data were fitted by the modified Curie-Weiss (CW) law

$$\chi(T) = \chi_0 + \frac{C}{T + \theta_{\text{CW}}}. \quad (4)$$

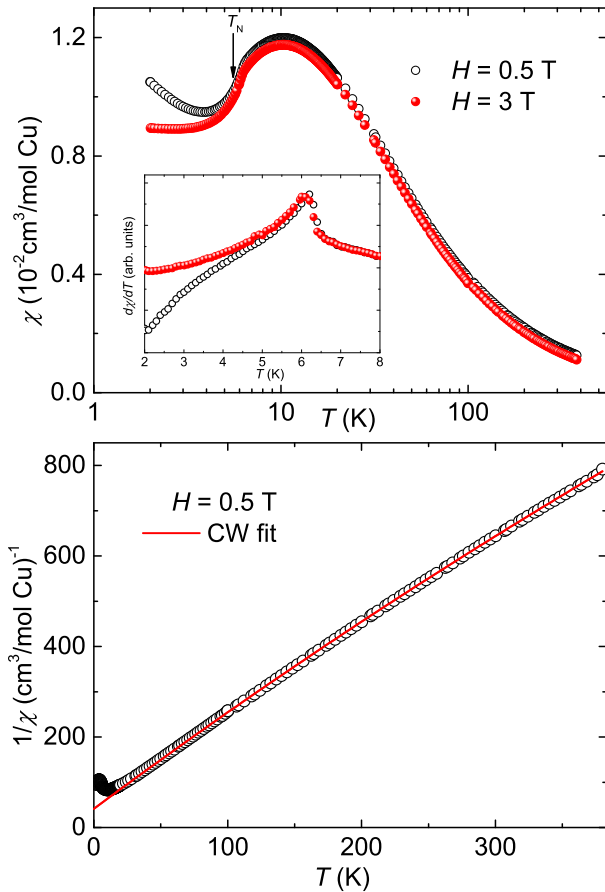


FIG. 4. Upper panel: temperature-dependent magnetic susceptibility $\chi(T)$ measured at different applied fields. Inset: $d\chi/dT$ vs temperature in the low-temperature regime to highlight the magnetic transition. Lower panel: inverse susceptibility ($1/\chi$) vs temperature and the solid line represents the fit using Eq. (4)

Here, χ_0 is the temperature-independent susceptibility, which includes Van-Vleck paramagnetism and core diamagnetism, and the second term is the CW law. Our fit in the high-temperature regime ($T \geq 100$ K) (see the lower panel of Fig. 4) yields the following parameters: $\chi_0 \simeq 1.42 \times 10^{-4} \text{ cm}^3/\text{mol-Cu}^{2+}$, the Curie constant $C \simeq 0.45 \text{ cm}^3\text{K}/\text{mol-Cu}^{2+}$, and the Curie-Weiss temperature $\theta_{\text{CW}} \simeq 18.7$ K. The core diamagnetic susceptibility χ_{core} of STCPO was calculated to be $-2.72 \times 10^{-4} \text{ cm}^3/\text{mol}$ by adding the core diamagnetic susceptibilities [16] of individual ions: Si^{2+} , Ti^{4+} , Cu^{2+} , P^{5+} , and O^{2-} . The Van-Vleck paramagnetic susceptibility χ_{VV} was estimated by subtracting χ_{dia} from χ_0 to be $\sim 4.14 \times 10^{-4} \text{ cm}^3/\text{mol}$. This value of χ_{VV} is close to the values reported for other cuprates [17, 18].

From the value of C , the effective moment is calculated to be $\mu_{\text{eff}} \simeq 1.89\mu_{\text{B}}$ using the relation $\mu_{\text{eff}} = \sqrt{3k_{\text{B}}C/N_{\text{A}}}$, where k_{B} is the Boltzmann constant and N_{A} is the Avogadro's number. This value of the effective moment corresponds to a Landé g -factor of $g \simeq 2.18$ [using

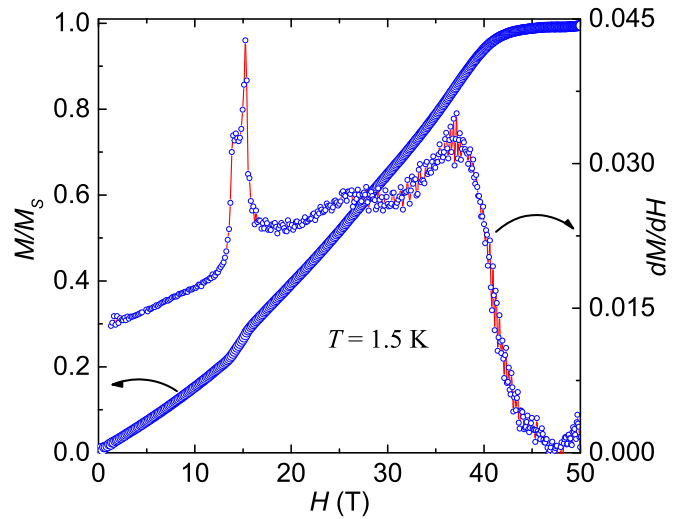


FIG. 5. Normalized magnetization isotherm (M vs H) at $T = 1.5$ K. dM/dH vs H is shown in the right y -axis.

$\mu_{\text{eff}} = g\sqrt{S(S+1)}\mu_{\text{B}}$. Such a large value of g is typically observed for powder samples containing magnetic Cu^{2+} ions. The positive value of θ_{CW} suggests that the dominant exchange interactions between Cu^{2+} ions are AFM in nature.

In order to study field-induced effects, magnetization isotherm (M vs H) was measured at $T = 1.5$ K up to 60 T. As shown in Fig. 5, M increases almost linearly with H and then exhibits a kink at $H \simeq 15$ T before reaching full saturation at $H_{\text{s}} \simeq 40$ T. The kink seems to occur around $\frac{1}{3}$ of the saturation magnetization (M_{s}). To visualize this feature, we plotted the derivative of M with respect to H i.e. dM/dH vs H in the right y -axis of Fig. 5, which shows a sharp peak at this field. The overall behavior of the M vs H curve is similar to that reported for BTCPO earlier [3].

C. Heat Capacity

The temperature-dependent heat capacity $C_{\text{p}}(T)$ is presented in Fig. 6. At high temperatures, C_{p} is dominated by phonon excitations. As the temperature is lowered, C_{p} shows a sharp λ -type anomaly at $T_{\text{N}} \simeq 6.2$ K, reflecting the magnetic LRO. Since a non-magnetic analogue compound could not be synthesized, we were unable to extract the magnetic part of the heat capacity from the total $C_{\text{p}}(T)$. Hence, no further analysis was possible. As shown in the upper inset of Fig. 6, a linear behavior was observed below T_{N} when C_{p}/T is plotted against $T^{3.2}$. Usually, in the three-dimensional (3D) ordered state, the spin-wave dispersion gives rise to a T^3 behavior for $C_{\text{p}}(T)$. The higher power-law exponent of 4.2 may indicate peculiarities of the magnetic excitation spectrum, such as the presence of a spin gap. However, we were unable to achieve a good fit of $C_{\text{p}}(T)$ assuming

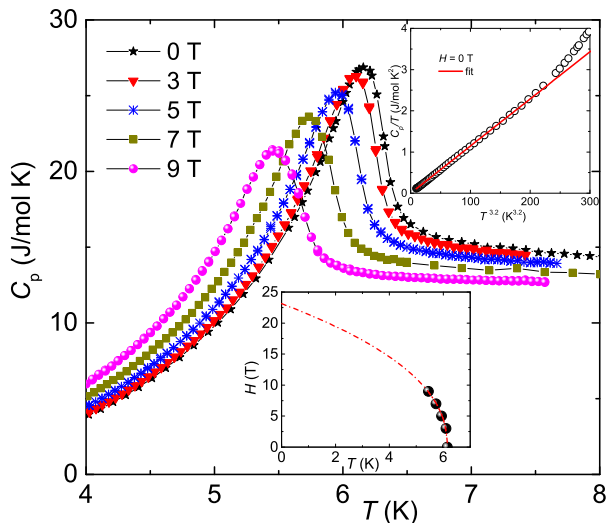


FIG. 6. $C_p(T)$ of STCPO measured at different applied fields in the low-temperature region around T_N . Upper inset: $C_p(T)/T$ vs $T^{3.2}$ at zero field, showing the linear regime below T_N . The solid line is the linear fit. Lower inset: H vs T_N phase diagram, with the dash-dotted line showing the fit using the power-law $H(T) = H_c \left(1 - \frac{T}{T_N}\right)^\beta$ and the extrapolation of this fit to low temperatures.

an activated behavior.

When the magnetic field is applied, the position of the anomaly at T_N shifts towards low temperatures, suggesting that the transition is AFM in nature. The variation of T_N with H is shown in the lower inset of Fig. 6, which is a typical phase diagram expected for an antiferromagnet. Field evolution can be described by an empirical power-law fit $H(T) = H_c \left(1 - \frac{T}{T_N}\right)^\beta$ with $H_c \simeq 23.1$ T, $T_N \simeq 6.15$ K, and $\beta \simeq 0.44$.

D. ^{31}P NMR

The crystal structure of STCPO features one P site. Two adjacent cupolas (one upward and one downward) in the ab -plane are connected through the PO_4 tetrahedra. Since P is strongly coupled with the Cu^{2+} ions, one can probe static and dynamic properties of Cu^{2+} spins via ^{31}P NMR.

1. ^{31}P NMR Shift

We observed a narrow spectral line above T_N as expected for an $I = 1/2$ nucleus [17, 19]. Figure 7 presents the ^{31}P NMR spectra measured at different temperatures. The line shape was found to be asymmetric, similar to that observed for $\text{Zn}_2\text{VO}(\text{PO}_4)_2$ because of the anisotropy in $\chi(T)$ and/or in the hyperfine coupling constant between the P nucleus and Cu^{2+} spins [20]. The

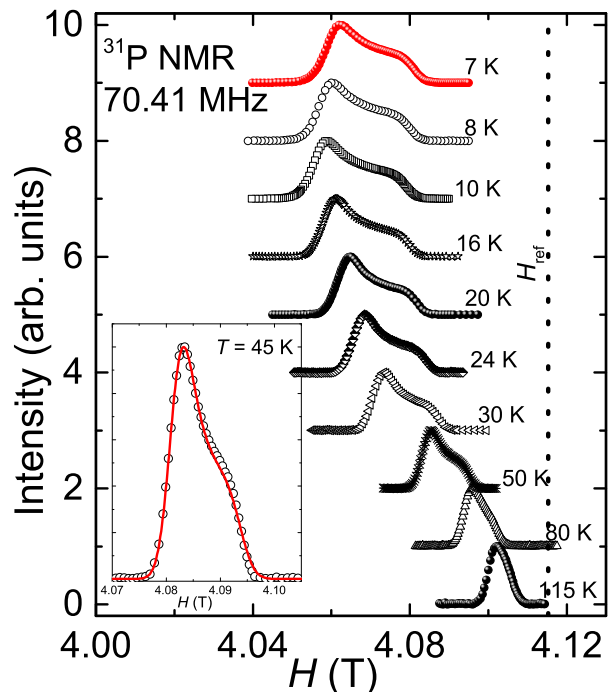


FIG. 7. (Color online) Field-sweep ^{31}P NMR spectra at different temperatures T ($T > T_N$) for the polycrystalline STCPO sample measured at 70.41 MHz. The vertical dashed line corresponds to the ^{31}P resonance frequency of the reference sample H_3PO_4 . Inset shows the ^{31}P NMR spectrum at 45 K (open circles). The solid line is the fit. The downward arrows point to the anisotropic shift values.

line position is found to shift with temperature. Temperature dependence of the NMR shift K extracted by fitting the spectra (see inset of Fig. 7) is presented in Fig. 8, which shows a strong anisotropy along different directions. At high temperatures, both isotropic (K_{iso}) and axial (K_{ax}) parts of the NMR shift vary in a Curie-Weiss manner and then pass through a broad maximum at around 10 K reflecting the low-dimensional short-range order, similar to the $\chi(T)$ data (Fig. 4).

The NMR shift $K(T)$ is a direct measure of the spin susceptibility χ_{spin} and is free from extrinsic contributions. Therefore, one can write $K(T)$ in terms of $\chi_{\text{spin}}(T)$ as

$$K(T) = K_0 + \frac{A_{\text{hf}}}{N_A} \chi_{\text{spin}}(T), \quad (5)$$

where K_0 is the temperature-independent chemical shift and A_{hf} is the hyperfine coupling constant between the P nuclei and Cu^{2+} electronic spins. The K vs χ plot with T as an implicit parameter is fitted very well by a straight line [Fig. 8 (lower panel)] over the whole temperature range ($T > T_N$) yielding the isotropic and axial parts of the hyperfine coupling $A_{\text{hf}}^{\text{iso}} \simeq 6539$ and $A_{\text{hf}}^{\text{ax}} \simeq 952$ Oe/ μ_B , respectively.

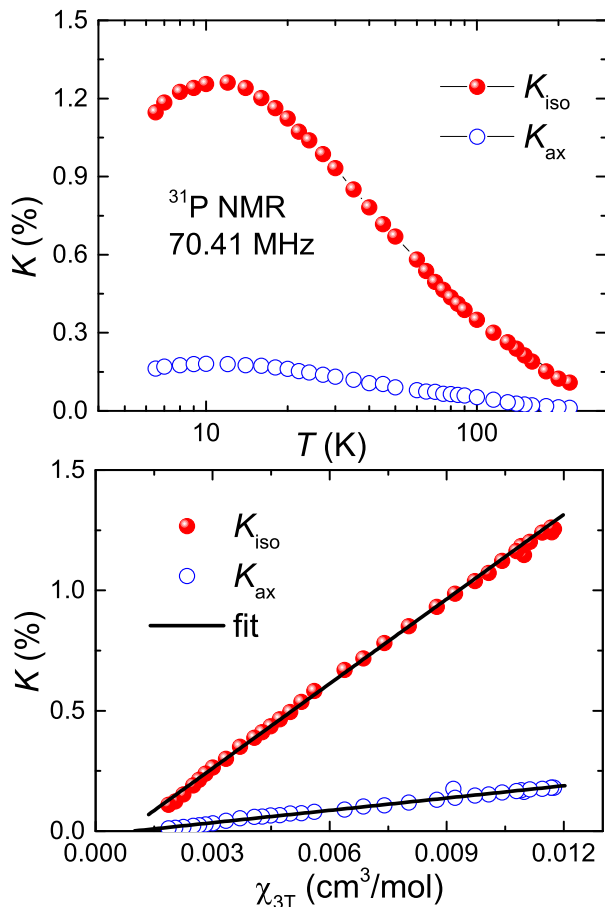


FIG. 8. (Color online) Upper panel: temperature-dependent isotropic and axial ^{31}P NMR shifts K_{iso} and K_{ax} vs T . Lower panel: ^{31}P NMR shift vs χ measured at 3 T is plotted with temperature as an implicit parameter for both K_{iso} and K_{ax} . The solid lines are linear fits.

2. NMR spectra below T_N

Below T_N , the ^{31}P spectra measured at 70.41 MHz were found to broaden abruptly and take a rectangular shape at very low temperatures. In order to precisely probe the intrinsic line shape, we re-measured the ^{31}P spectra at a lower frequency of 25 MHz. As shown in Fig. 9, the ^{31}P line above T_N remains narrow and immediately below T_N it starts broadening indicating that the P site is experiencing the static internal field in the ordered state through the hyperfine field between the P nuclei and the ordered Cu^{2+} moments. Below about 4 K, it becomes nearly rectangular with the center of gravity at 1.44 T, which is the resonance field for the ^{31}P nuclei. It is well documented that for a polycrystalline sample, in a commensurate ordered state, the direction of the internal field is randomly distributed with respect to the applied field and one gets a rectangular spectral shape [23, 24]. Indeed, such rectangular spectra have been observed in several compounds in the commensurate AFM ordered state. On the other hand, for an incommensurate ordered

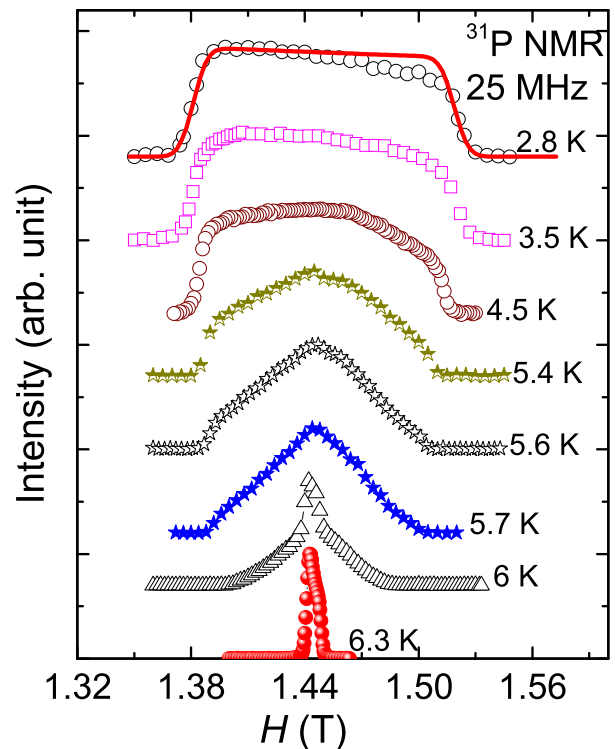


FIG. 9. (Color online) Temperature-dependent ^{31}P NMR spectra measured at 25 MHz below T_N . The solid line is the fit to the spectrum at $T = 2.8$ K as in Refs. 21 and 22. The spectra in the paramagnetic state broaden below T_N and take a rectangular shape due to the internal field H_{int} .

state, the NMR line shape is expected to be nearly triangular [25]. In an attempt to fit our spectrum at 2.8 K, we followed the procedure adopted in Ref. 22. The simulated spectra (see the solid line in Fig. 9) reproduce the experimental line shape very well, confirming the commensurate nature of the ordering below T_N .

The internal field H_{int} , which is proportional to the Cu^{2+} sublattice magnetization, was determined by taking the half-width at half-maximum. The temperature dependence of H_{int} is plotted in Fig. 10. In order to extract the critical exponent (β) of the order parameter, $H_{\text{int}}(T)$ was fitted by the power law of the form:

$$H_{\text{int}}(T) = H_0 \left(1 - \frac{T}{T_N}\right)^\beta. \quad (6)$$

H_{int} decreases rapidly on approaching T_N . For an accurate estimation of β , one needs more data points close to T_N . We have estimated β by fitting the data points in the critical region (close to T_N) as shown in Fig. 10. The value of $\beta \simeq 0.38$ with $H_0 \simeq 0.124$ T and $T_N \simeq 6.04$ K was obtained by fitting the data points in the T -range 5 K to 6 K, close to T_N . In order to highlight the fit in the critical region, H_{int} is plotted against the reduced temperature, $\tau = 1 - \frac{T}{T_N}$ in the inset of Fig. 10. The solid line is the fit by $0.124 \times \tau^{0.38}$ where T_N is taken to be 6.04 K. At low temperatures, H_{int} develops the tendency toward

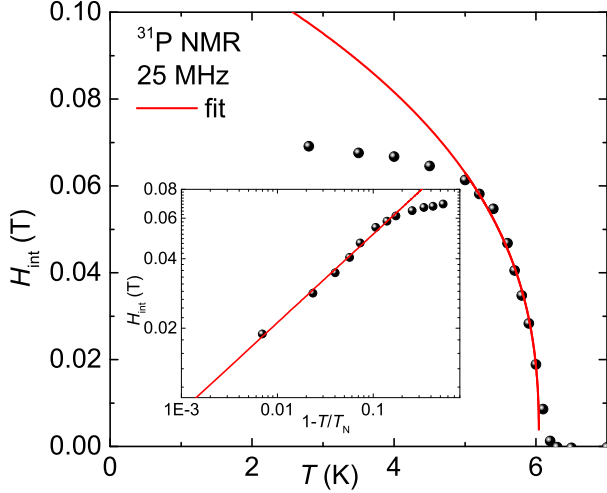


FIG. 10. (Color online) Temperature dependence of the internal field H_{int} obtained from NMR spectra measured at 25 MHz in the ordered state. The solid line is the fit by Eq. (6) as described in the text. Inset: $H_{\text{int}} \text{ vs } \tau$.

saturation and saturates faster than expected from the mean-field theory [see the deviation of fits in Fig. 10 at low- T s].

Usually, the critical exponent β reflects the universality class of a spin system. The β values expected for different spin- and lattice-dimensionalities are listed in Ref. 26. Our experimental value of $\beta \approx 0.38$ is somewhat higher than any of the 3D spin models (Heisenberg, Ising, or XY) suggesting that the magnetic ordering is not driven by simple 3D correlations. This further corroborates our previous assessment based on the $C_p(T)$ data.

3. Nuclear spin-lattice relaxation rate $1/T_1$

The ^{31}P nuclear spin-lattice relaxation rate $1/T_1$ above T_N was measured at the field corresponding to the central peak position. For an $I = 1/2$ nucleus, the recovery of the longitudinal magnetization is expected to follow a single-exponential behavior. Indeed, our recovery curves were fitted well by the exponential function

$$1 - \frac{M(t)}{M_0} = Ae^{-t/T_1}, \quad (7)$$

where $M(t)$ is the nuclear magnetization at a time t after the saturation pulse and M_0 is the equilibrium magnetization. The temperature dependence of $1/T_1$ extracted from the fit is presented in Fig. 11.

The $1/T_1$ data measured at two different frequencies (70.41 MHz and 25 MHz) almost resemble each other at low temperatures. At high temperatures ($T \gtrsim 30$ K), $1/T_1$ is temperature-independent. In the paramagnetic limit $T \gg J/k_B$, a temperature-independent $1/T_1$ behavior is typically expected due to uncorrelated moments [27]. As the temperature is lowered, $1/T_1$ decreases

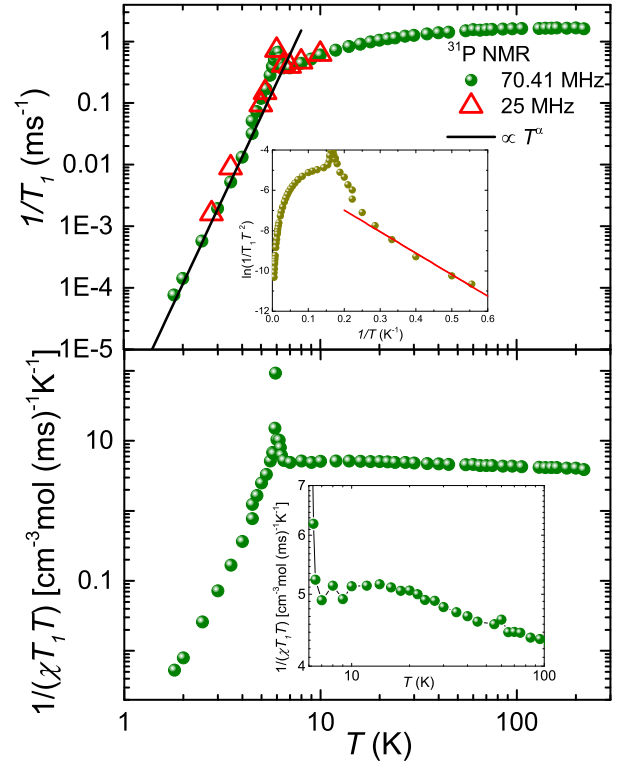


FIG. 11. (Color online) Upper panel: spin-lattice relaxation rate $1/T_1$ vs temperature T measured at 70.41 and 25 MHz. The solid line represents the fit in the low-temperature region by $1/T_1 \propto T^\alpha$ with $\alpha \simeq 6.8$. Inset: $\ln(1/T_1 T^2)$ vs $1/T$ and the solid line is the linear fit below T_N . Lower panel: $1/(\chi T_1 T)$ is plotted as a function of T for 70.41 MHz. Inset: magnified $1/(\chi T_1 T)$ vs T plot above T_N .

slowly for $T < 20$ K and then shows a weak anomaly around $T_N \simeq 6.2$ K. Similar decrease has also been reported earlier for some low-dimensional antiferromagnets $\text{Pb}_2\text{VO}(\text{PO}_4)_2$ [26], $\text{SrZnVO}(\text{PO}_4)_2$ [28], VOMoO_4 [29], and $[\text{Cu}(\text{HCO}_2)_2 \cdot 4\text{D}_2\text{O}]$, where the decrease of $1/T_1$ above T_N is explained by the cancellation of the antiferromagnetic spin fluctuations at the probed nuclei [30]. Below T_N , $1/T_1$ again decreases smoothly towards zero.

In the lower panel of Fig. 11, $1/(\chi T_1 T)$ is plotted against temperature. For $T \geq 30$ K, it shows a temperature-independent behavior, and a slow increase was observed just below 30 K where the system begins to show an AFM short-range order. In the inset of Fig. 11, the data above T_N is magnified in order to highlight the slow increase. The general expression for $1/(T_1 T)$ in terms of the dynamic susceptibility $\chi_M(\mathbf{q}, \omega_0)$ can be written as [31, 32]

$$\frac{1}{T_1 T} = \frac{2\gamma_N^2 k_B}{N_A^2} \sum_{\vec{q}} |A(\mathbf{q})|^2 \frac{\chi''_M(\mathbf{q}, \omega_0)}{\omega_0}, \quad (8)$$

where the sum is over wave vectors \vec{q} within the first Brillouin zone, $A(\mathbf{q})$ is the form-factor of the hyperfine interactions as a function of \mathbf{q} , and $\chi''_M(\mathbf{q}, \omega_0)$ is the imaginary

part of the dynamic susceptibility at the nuclear Larmor frequency ω_0 . For $q = 0$ and $\omega_0 = 0$, the real component of $\chi'_M(\mathbf{q}, \omega_0)$ corresponds to the uniform static susceptibility χ . Thus the temperature-independent $1/(\chi T_1 T)$ above 30 K in Fig. 11 (bottom panel) demonstrates the dominant contribution of χ to $1/T_1 T$. On the other hand, a slight increase in $1/(\chi T_1 T)$ below 30 K indicates the growth of AFM correlations with decreasing T , which is typically observed in frustrated magnets.

In the magnetically ordered state ($T < T_N$), the strong temperature dependence of $1/T_1$ is a clear signature of the relaxation due to scattering of magnons by the nuclear spins [33]. For $T \gg \Delta/k_B$, $1/T_1$ follows either a T^3 behavior or a T^5 behavior due to a two-magnon Raman process or a three-magnon process, respectively, where Δ is the energy gap in the spin-wave excitation spectrum [21, 34]. At very low temperatures ($T \ll \Delta/k_B$), it follows an activated behavior $1/T_1 \propto T^2 e^{-\Delta/k_B T}$. As shown in the upper panel of Fig. 11, $1/T_1$ below T_N follows a power law ($\propto T^\alpha$) with an unusually large value $\alpha \simeq 6.8$. In order to check whether there may exist a magnon gap, we have plotted $\ln(1/T_1 T^2)$ vs $1/T$ in the upper inset of Fig. 11. Indeed, it shows a linear regime below ~ 3.5 K and a straight line fit below 3.5 K yields the gap value $\Delta/k_B \simeq 10.6$ K. This is consistent with the unusually high power-law in the heat capacity, although, as previously mentioned, no clear activated behavior could be seen in $C_p(T)$.

E. Microscopic magnetic model

Exchange couplings were calculated for the experimental crystal structure reported in Ref. 1. First, we mapped valence bands formed by the half-filled Cu orbitals onto a tight-binding model and estimated the hopping parameters t_i (Table I), which define AFM superexchange interactions as $J_i^{\text{AFM}} = 4t_i^2/U_{\text{eff}}$, where U_{eff} is the effective on-site Coulomb repulsion in the Cu 3d bands. This way, the overall span of the exchange couplings is probed.

The spin lattice of $\text{Sr}(\text{TiO})\text{Cu}_4(\text{PO}_4)_4$ comprises square cupola with the leading nearest-neighbor coupling J . A weaker and frustrating second-neighbor coupling J_2 may exist too. Several superexchange pathways are present between the cupola. Among them, the second-neighbor ("diagonal") J' is clearly more efficient than the nearest-neighbor J_1 and J'_1 (Fig. 12). The leading inter-plane coupling runs perpendicular to the ab plane via $t_\perp \simeq 5$ meV that corresponds to a minute $J_\perp^{\text{AFM}} \simeq 0.3$ K assuming $U_{\text{eff}} = 4$ eV [11].

DFT+ U calculations give access to absolute values of the exchange couplings, including both FM and AFM contributions (Table I). They confirm the leading coupling J , the presence of the frustrating second-neighbor coupling J_2 within the cupolas and the non-frustrated coupling J' between them. Therefore, the minimum magnetic model comprises isolated square cupolas with only the nearest-neighbor coupling J . As a better approxima-

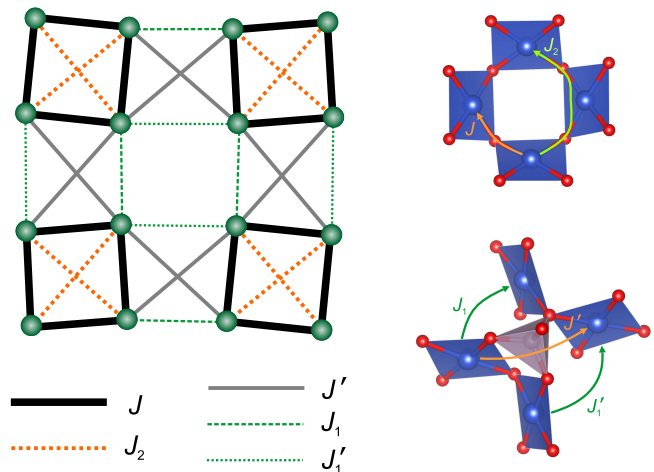


FIG. 12. Spin lattice of $\text{Sr}(\text{TiO})\text{Cu}_4(\text{PO}_4)_4$ and mechanisms of individual exchange couplings. Note that the Cu-O...O-Cu superexchange pathway of J' is more straight than those of J_1 and J'_1 .

TABLE I. Calculated exchange couplings in $\text{Sr}(\text{TiO})\text{Cu}_4(\text{PO}_4)_4$: the interatomic distances $d_{\text{Cu-Cu}}$ (in Å), hopping parameters t_i (in meV), and total exchange couplings J_i (in K) obtained from DFT+ U with $U_d = 9.5$ eV and $J_d = 1$ eV.

	$d_{\text{Cu-Cu}}$	t_i	J_i
J	3.147	118	27.9
J_1	3.619	23	1.0
J'_1	4.101	-9	0.0
J_2	4.450	14	5.8
J'	4.973	-48	7.0
J'_2	5.097	10	2.2

tion, the couplings J_2 and J' should be included.

The model of isolated cupolas with only nearest-neighbor couplings describes the susceptibility down to 30 K but clearly fails to reproduce the position and height of the maximum (Fig. 13, dashed line). Including J' improves the fit down to about 20 K. However, the main improvement is achieved by including J_2 that, even in the absence of J' , describes the data down to 14 K. By combining J' and J_2 , we get the best fit using $J = 16.3$ K, $J_2/J = 1.0$, and $J'/J = 0.6$ down to 8.5 K. Both position and height of the maximum are well reproduced (Fig. 13, solid line). The fitted g -value of 2.17 seems realistic for Cu^{2+} and consistent with $g = 2.18$ from the Curie-Weiss fit.

Same exchange parameters were used to simulate the magnetization process of $\text{Sr}(\text{TiO})\text{Cu}_4(\text{PO}_4)_4$ and lead to a good agreement with the experimental saturation field (Fig. 13, inset). However, finite-size effects are significant, and not all features of the experimental curve are reproduced, because the transition around 15 T is anisotropic in nature [3] and can not be captured on the

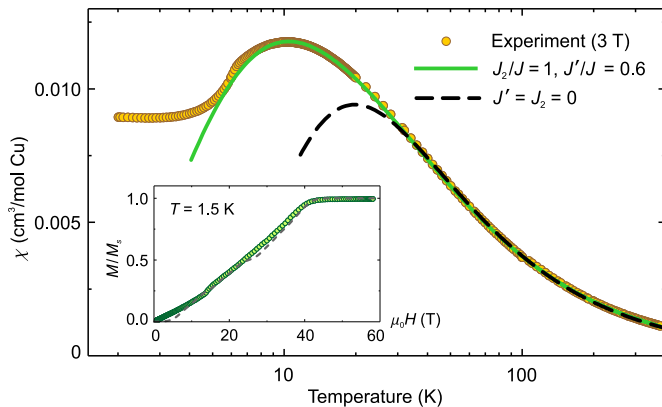


FIG. 13. Magnetic susceptibility of $\text{Sr}(\text{TiO})\text{Cu}_4(\text{PO}_4)_4$ (circles) and the fits within the models of isolated square cupolas ($J = 25.3 \text{ K}$, $J_2 = J' = 0$, $g = 2.14$, dashed line) and coupled frustrated cupolas ($J = 16.3 \text{ K}$, $J_2/J = 1.0$, $J'/J = 0.6$, $g = 2.17$, solid line). The inset shows experimental magnetization curve (circles) and the simulation using the latter model at $T/J = 0.1$ (short-dashed line). The bends in the simulated curve are due to finite-size effects.

level of Heisenberg spin Hamiltonian.

IV. DISCUSSION AND CONCLUSIONS

Similar to BTCPO, the spin lattice of STCPO comprises square cupolas. However, the nearest-neighbor coupling within the cupolas is by far insufficient to describe magnetic susceptibility of this compound. Our fits show that the second-neighbor coupling J_2 and the coupling J' between the cupolas are both sizable and integral to the magnetic model.

The moderate size of J , 27.9 K in DFT and 16.3 K in the experiment, is controlled by the Cu-O-Cu angle of 107.4° [1] that lies on the border between FM and AFM superexchange. In this range of the bridging angles, subtle structural details, as well as side groups, have strong influence on the absolute value and even on the sign of the coupling [11, 35, 36]. In BTCPO, a somewhat larger nearest-neighbor coupling of $J = 35 \text{ K}$ was reported [2, 3]. Indeed, the Ba compound systematically shows higher values of $T_N \simeq 9.5 \text{ K}$ [2] (vs. 6.2 K), $T_\chi^{\text{max}} \simeq 15 \text{ K}$ [2] (vs. 10 K), and $H_s \simeq 60 \text{ T}$ [3] (vs. 40 T). Here, the values in brackets are for the Sr compound reported in this work.

The second-neighbor coupling J_2 is more unusual, because its experimental value of about 16 K is much larger than 5 K found in DFT. One plausible explanation for this discrepancy would be subtle structural changes upon cooling, as room-temperature crystal structure was used in DFT calculations for the lack of any crystallographic information at lower temperatures. The mechanism of J_2 should involve $\text{Cu-O}\dots\text{O-Cu}$ superexchange mediated

by the relatively short $\text{O}\dots\text{O}$ distance of 2.76 \AA along the edge of the CuO_4 plaquette. A similar mechanism should be relevant to the couplings J' , J_1 , and J'_1 , but the shorter $\text{O}\dots\text{O}$ contact of $2.48 - 2.51 \text{ \AA}$ is along the edge of the PO_4 tetrahedron in this case. The size of the coupling is controlled by deviations from linearity quantified by the deviation of the Cu-O-O angles from 180° [37–39]. The strongest coupling J' is found for the least curved $\text{Cu-O}\dots\text{O-Cu}$ superexchange pathway (Fig. 12).

Magnetic response of STCPO reveals several peculiarities. First, the magnetic ordering transition at $T_N \simeq 6.2 \text{ K}$ is observed well below the susceptibility maximum at $T_\chi^{\text{max}} \simeq 10 \text{ K}$, and the ratio $\theta_{\text{CW}}/T_N = 3.0$ indicates a sizable reduction in T_N due to the low-dimensionality and frustration. Second, the long-range-ordered state appears to be commensurate, but both specific heat and $1/T_1$ decrease rapidly at low temperatures. This may indicate gapped nature of magnetic excitations.

A somewhat different coupling regime was reported for BTCPO in previous studies. The authors of Refs. 2 and 3 argue that J' is about 50% of J , whereas J_2 is only a minor coupling ($J_2/J = \frac{1}{6}$). We note, however, that these values were not tested against the experimental magnetic susceptibility, and only a classical analysis of the spin model was performed [3]. Gapped magnetic excitations may be related to the non-negligible anisotropy postulated for the Ba compound. On the other hand, the coupling J_2 can play a role in the stabilization of the non-coplanar state, an effect hitherto ascribed to the Dzyaloshinsky-Moriya anisotropy [3].

In summary, we explored the low-temperature behavior of $\text{Sr}(\text{TiO})\text{Cu}_4(\text{PO}_4)_4$, a quantum magnet comprising the square cupolas of Cu^{2+} ions. Our results indicate sizable couplings between individual cupola units, as well as strong frustration within the cupolas. A spin gap of about 10 K may form in the ordered state, resulting in the unusually high power-law exponent of the specific heat and the activated behavior of the spin-lattice relaxation rate at low temperatures.

Note Added: after the submission of our work, Kimura *et al.* [40] reported the magnetic structure of STCPO from neutron diffraction experiments. Their commensurate magnetic structure is consistent with our NMR data. Additionally, STCPO shows a pronounced dielectric anomaly at T_N but no ferroelectricity was observed.

ACKNOWLEDGMENTS

SSI and RN would like to acknowledge BRNS, India for financial support bearing sanction No.37(3)/14/26/2017-BRNS. AT acknowledges financial support by the Federal Ministry for Education and Research via the Sofja Kovalevskaya Award of Alexander von Humboldt Foundation.

- [1] K. Kimura, M. Sera, and T. Kimura, “ A^{2+} cation control of chiral domain formation in $A(\text{TiO})\text{Cu}_4(\text{PO}_4)_4$ ($A = \text{Ba}, \text{Sr}$),” *Inorg. Chem.* **55**, 1002–1004 (2016).
- [2] K. Kimura, P. Babkevich, M. Sera, M. Toyoda, K. Yamauchi, G. S. Tucker, J. Martius, T. Fennell, P. Manuel, D. D. Khalyavin, R. D. Johnson, T. Nakano, Y. Nozue, H. M. Rønnow, and T. Kimura, “Magnetodielectric detection of magnetic quadrupole order in $\text{Ba}(\text{TiO})\text{Cu}_4(\text{PO}_4)_4$ with Cu_4O_{12} square cupolas,” *Nature Comm.* **7**, 13039 (2016).
- [3] Y. Kato, K. Kimura, A. Miyake, M. Tokunaga, A. Matsuo, K. Kindo, M. Akaki, M. Hagiwara, M. Sera, T. Kimura, and Y. Motome, “Magnetoelectric behavior from $S = \frac{1}{2}$ asymmetric square cupolas,” *Phys. Rev. Lett.* **118**, 107601 (2017).
- [4] K. Kenta, S. Masakazu, N. Takehito, N. Yasuo, and K. Tsuyoshi, “Magnetodielectric properties of the square cupola antiferromagnet $\text{Ba}(\text{TiO})\text{Cu}_4(\text{PO}_4)_4$,” *Physica B* **536**, 93–95 (2017).
- [5] P. Babkevich, L. Testa, K. Kimura, T. Kimura, G. S. Tucker, B. Roessli, and H. M. Rønnow, “Magnetic structure of $\text{Ba}(\text{TiO})\text{Cu}_4(\text{PO}_4)_4$ probed using spherical neutron polarimetry,” *Phys. Rev. B* **96**, 214436 (2017).
- [6] A. A. Tsirlin, B. Schmidt, Y. Skourski, R. Nath, C. Geibel, and H. Rosner, “Exploring the spin- $\frac{1}{2}$ frustrated square lattice model with high-field magnetization studies,” *Phys. Rev. B* **80**, 132407 (2009).
- [7] K. Koepf and H. Eschrig, “Full-potential nonorthogonal local-orbital minimum-basis band-structure scheme,” *Phys. Rev. B* **59**, 1743–1757 (1999).
- [8] J. P. Perdew, K. Burke, and M. Ernzerhof, “Generalized gradient approximation made simple,” *Phys. Rev. Lett.* **77**, 3865–3868 (1996).
- [9] H. J. Xiang, E. J. Kan, S.-H. Wei, M.-H. Whangbo, and X. G. Gong, “Predicting the spin-lattice order of frustrated systems from first principles,” *Phys. Rev. B* **84**, 224429 (2011).
- [10] O. Janson, I. Rousochatzakis, A. A. Tsirlin, J. Richter, Yu. Skourski, and H. Rosner, “Decorated Shastry-Sutherland lattice in the spin-1/2 magnet $\text{CdCu}_2(\text{BO}_3)_2$,” *Phys. Rev. B* **85**, 064404 (2012).
- [11] R. Nath, A. A. Tsirlin, P. Khuntia, O. Janson, T. Förster, M. Padmanabhan, J. Li, Yu. Skourski, M. Baenitz, H. Rosner, and I. Rousochatzakis, “Magnetization and spin dynamics of the spin $S = 1/2$ hourglass nanomagnet $\text{Cu}_5(\text{OH})_2(\text{NIPA})_4 \cdot 10\text{H}_2\text{O}$,” *Phys. Rev. B* **87**, 214417 (2013).
- [12] S. Lebernegg, A. A. Tsirlin, O. Janson, and H. Rosner, “Spin gap in malachite $\text{Cu}_2(\text{OH})_2\text{CO}_3$ and its evolution under pressure,” *Phys. Rev. B* **88**, 224406 (2013).
- [13] A.F. Albuquerque, F. Alet, P. Corboz, P. Dayal, A. Feiguin, S. Fuchs, L. Gamper, E. Gull, S. Gürtler, A. Honecker, R. Igarashi, M. Körner, A. Kozhevnikov, A. Läuchli, S.R. Manmana, M. Matsumoto, I.P. McCulloch, F. Michel, R.M. Noack, G. Pawłowski, L. Pollet, T. Pruschke, U. Schollwöck, S. Todo, S. Trebst, M. Troyer, P. Werner, and S. Wessel, “The ALPS project release 1.3: Open-source software for strongly correlated systems,” *J. Magn. Magn. Mater.* **310**, 1187–1193 (2007).
- [14] J. Rodríguez-Carvajal, “Recent advances in magnetic structure determination by neutron powder diffraction,” *Physica B* **192**, 55–69 (1993).
- [15] S. Pakhira, C. Mazumdar, R. Ranganathan, S. Giri, and M. Avdeev, “Large magnetic cooling power involving frustrated antiferromagnetic spin-glass state in R_2NiSi_3 ($\text{R} = \text{Gd}, \text{Er}$),” *Phys. Rev. B* **94**, 104414 (2016).
- [16] P. W. Selwood, *Magnetochemistry* (Interscience, New York, 1956).
- [17] R. Nath, A. V. Mahajan, N. Büttgen, C. Kegler, A. Loidl, and J. Bobroff, “Study of one-dimensional nature of $S = \frac{1}{2}$ $(\text{Sr}, \text{Ba})_2\text{Cu}(\text{PO}_4)_2$ and BaCuP_2O_7 via ^{31}P NMR,” *Phys. Rev. B* **71**, 174436 (2005).
- [18] N. Motoyama, H. Eisaki, and S. Uchida, “Magnetic susceptibility of ideal spin- $\frac{1}{2}$ Heisenberg antiferromagnetic chain systems, Sr_2CuO_3 and SrCuO_2 ,” *Phys. Rev. Lett.* **76**, 3212–3215 (1996).
- [19] R. Nath, Deepa Kasinathan, H. Rosner, M. Baenitz, and C. Geibel, “Electronic and magnetic properties of $\text{K}_2\text{CuP}_2\text{O}_7$: A model $S = \frac{1}{2}$ Heisenberg chain system,” *Phys. Rev. B* **77**, 134451 (2008).
- [20] A. Yogi, N. Ahmed, R. Nath, A. A. Tsirlin, S. Kundu, A. V. Mahajan, J. Sichelschmidt, B. Roy, and Y. Furukawa, “Antiferromagnetism of $\text{Zn}_2\text{VO}(\text{PO}_4)_2$ and the dilution with Ti^{4+} ,” *Phys. Rev. B* **91**, 024413 (2015).
- [21] R. Nath, K. M. Ranjith, B. Roy, D. C. Johnston, Y. Furukawa, and A. A. Tsirlin, “Magnetic transitions in the spin- $\frac{5}{2}$ frustrated magnet BiMn_2PO_6 and strong lattice softening in BiMn_2PO_6 and BiZn_2PO_6 below 200 K,” *Phys. Rev. B* **90**, 024431 (2014).
- [22] K. M. Ranjith, R. Nath, M. Majumder, D. Kasinathan, M. Skoulatos, L. Keller, Y. Skourski, M. Baenitz, and A. A. Tsirlin, “Commensurate and incommensurate magnetic order in spin-1 chains stacked on the triangular lattice in $\text{Li}_2\text{NiW}_2\text{O}_8$,” *Phys. Rev. B* **94**, 014415 (2016).
- [23] Y. Yoshihiro and S. Akihiko, “An analysis method of antiferromagnetic powder patterns in spin-echo NMR under external fields,” *J. Phys. Soc. Jpn.* **55**, 1751–1758 (1986).
- [24] J. Kikuchi, K. Ishiguchi, K. Motoya, M. Itoh, K. Inari, N. Eguchi, and J. Akimitsu, “NMR and neutron scattering studies of quasi one-dimensional magnet CuV_2O_6 ,” *J. Phys. Soc. Jpn.* **69**, 2660–2668 (2000).
- [25] M. Kontani, T. Hioki, and Y. Masuda, “Hyperfine fields in an incommensurate antiferromagnetic Cr-Mo alloy system,” *J. Phys. Soc. Jpn.* **39**, 672–674 (1975).
- [26] R. Nath, Y. Furukawa, F. Borsa, E. E. Kaul, M. Baenitz, C. Geibel, and D. C. Johnston, “Single-crystal ^{31}P NMR studies of the frustrated square-lattice compound $\text{Pb}_2(\text{VO})(\text{PO}_4)_2$,” *Phys. Rev. B* **80**, 214430 (2009).
- [27] T. Moriya, “Nuclear magnetic relaxation in antiferromagnetics,” *Prog. Theor. Phys.* **16**, 23–44 (1956).
- [28] L. Bossoni, P. Carretta, R. Nath, M. Moscardini, M. Baenitz, and C. Geibel, “NMR and μSR study of spin correlations in $\text{SrZnVO}(\text{PO}_4)_2$: An $S = \frac{1}{2}$ frustrated magnet on a square lattice,” *Phys. Rev. B* **83**, 014412 (2011).
- [29] P. Carretta, N. Papinutto, C. B. Azzoni, M. C. Mozzati, E. Pavarini, S. Gonthier, and P. Millet, “Frustration-driven structural distortion in VOMoO_4 ,” *Phys. Rev. B* **66**, 094420 (2002).
- [30] P. Carretta, T. Ciabattini, A. Cucchi, E. Mognaschi, A. Rigamonti, V. Tognetti, and P. Verrucchi, “Spin dynamics and magnetic correlation length in

- two-dimensional quantum Heisenberg antiferromagnets,” *Phys. Rev. Lett.* **84**, 366–369 (2000).
- [31] T. Moriya, “The effect of electron-electron interaction on the nuclear spin relaxation in metals,” *J. Phys. Soc. Jpn.* **18**, 516–520 (1963).
- [32] A. V. Mahajan, R. Sala, E. Lee, F. Borsa, S. Kondo, and D. C. Johnston, “ ^7Li and ^{51}V NMR structure of the heavy-fermion compound LiV_2O_4 ,” *Phys. Rev. B* **57**, 8890–8899 (1998).
- [33] M. Belesi, F. Borsa, and A. K. Powell, “Evidence for spin-wave excitations in the long-range magnetically ordered state of a Fe_{19} molecular crystal from proton NMR,” *Phys. Rev. B* **74**, 184408 (2006).
- [34] D. Beeman and P. Pincus, “Nuclear spin-lattice relaxation in magnetic insulators,” *Phys. Rev.* **166**, 359–375 (1968).
- [35] S. Lebernegg, O. Janson, I. Rousochatzakis, S. Nishimoto, H. Rosner, and A.A. Tsirlin, “Frustrated spin chain physics near the Majumdar-Ghosh point in szenic-site $\text{Cu}_3(\text{MoO}_4)(\text{OH})_4$,” *Phys. Rev. B* **95**, 035145 (2017).
- [36] D. I. Badrtdinov, E. S. Kuznetsova, V. Yu. Verchenko, P. S. Berdonosov, V. A. Dolgikh, V. V. Mazurenko, and A. A. Tsirlin, “Magnetism of coupled spin tetrahedra in ilinskite-type $\text{KCu}_5\text{O}_2(\text{SeO}_3)_2\text{Cl}_3$,” *Sci. Reports* **8**, 2379 (2018).
- [37] A. A. Tsirlin and H. Rosner, “Microscopic model of $(\text{CuCl})\text{LaNb}_2\text{O}_7$: Coupled spin dimers replace a frustrated square lattice,” *Phys. Rev. B* **82**, 060409(R) (2010).
- [38] R. Nath, K. M. Ranjith, J. Sichelschmidt, M. Baenitz, Y. Skourski, F. Alet, I. Rousochatzakis, and A. A. Tsirlin, “Hindered magnetic order from mixed dimensionalities in CuP_2O_6 ,” *Phys. Rev. B* **89**, 014407 (2014).
- [39] P. S. Berdonosov, O. Janson, A. V. Olenev, S. V. Krivovichev, H. Rosner, V. A. Dolgikh, and A. A. Tsirlin, “Crystal structures and variable magnetism of $\text{PbCu}_2(\text{XO}_3)_2\text{Cl}_2$ with $\text{X} = \text{Se}, \text{Te}$,” *Dalton Trans.* **42**, 9547 (2013).
- [40] K. Kimura, M. Toyoda, P. Babkevich, K. Yamauchi, M. Sera, V. Nassif, H. M. Rønnow, and T. Kimura, “A-cation control of magnetoelectric quadrupole order in $\text{A}(\text{TiO})\text{Cu}_4(\text{PO}_4)_4$ ($\text{A} = \text{Ba}, \text{Sr}, \text{and Pb}$),” *Phys. Rev. B* **97**, 134418 (2018).